Article

Direct Crystallization Resolution of Racemates Enhanced by Chiral Nanorods: Experimental, Statistical, and Quantum Mechanics/ Molecular Dynamics Simulation Studies

Jiaojiao Cao,[||] Boxuan Lou,[||] Yue Xu,[||] Xiaolan Qin, Haikuan Yuan, Lijuan Zhang, Yan Zhang, Sohrab Rohani, and Jie Lu*

Read Online

ACCESS | Metrics & More | Article Recommendations | Supporting Information

ABSTRACT: Three chiral nanorods of C_{14}-L-Thea, C_{14}-L-Phe, and C_{14}-D-Phe were first synthesized and utilized as heterogeneous nucleants to enhance the resolution of racemic Asp via direct crystallization. Through the statistical analysis from 320 batches of nucleation experiments, we found that the apparent appearance diversity of two enantiomeric crystals of Asp existed in 80 homogeneous experiments without chiral nanorods. However, in 240 heterogeneous experiments with 4.0 wt % chiral nanorods of solute mass added, the appearance of those nuclei with the same chirality as the nanorods was apparently promoted, and that with the opposite chirality was totally inhibited. Under a supersaturation level of 1.08, the maximum ee of the initial nuclei was as high as

23.51%. When the cooling rate was 0.025 K/min, the ee of the product was up to 76.85% with a yield of 14.41%. Furthermore, the simulation results from quantum mechanics (QM) and molecular dynamics (MD) revealed that the higher chiral recognition ability of C_{14}-L-Thea compared to C_{14}-L-Phe that originated from the interaction difference between C_{14}-L-Thea and Asp enantiomers was larger than that between C_{14}-L-Phe and Asp enantiomers. Moreover, the constructed nanorods exhibited good stability and recyclability.
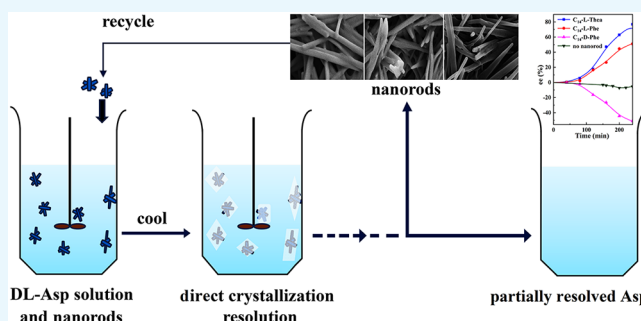
1. INTRODUCTION

Chirality exists universally with diverse forms at all levels.[1] In an achiral environment, mutual enantiomers have the same chemical and physical characteristics but often possess different performances in a chiral environment. Therefore, in many fields, particularly the pharmaceutical industry, it is critical to manufacture pure enantiomeric compounds.[2,3] At present, practical technologies to prepare pure enantiomers include chiral separation[4] and asymmetric synthesis.[5] Although the asymmetric synthesis is the main method for the preparation of enantiomers, it generally suffers from the disadvantage that the product frequently has a lower enantiomeric excess (ee) and accordingly requires further enrichment.[6,7] For some chiral systems, the preparation of enantiomers through the separation of racemates has obvious advantages, particularly including that the multifarious selection of expensive and suitable catalysts is unnecessary.[8] The emerged chiral separation techniques involve membrane separation,[9,10] chromatographic separation,[11] enzymatic kinetic resolution,[12] crystallization,[13,14] liquid−liquid extraction,[15] etc.

Specifically, crystallization is widely utilized to resolve racemates as well as to purify enantiomers in a large scale because its operation is convenient, economical, and widely applicable.[16] Nowadays, the frequently used crystallization

resolution methods include preferential crystallization,[17] diastereomer crystallization,[18] spontaneous crystallization,[19] and that using tailor-made additives[20] or nucleants.[21] Among them, the diastereomeric approach is the most verbose to produce optically pure enantiomers by means of sequential steps. On the contrary, direct crystallization for racemates promoted by crystal seeds, additives, or nucleants has been emerging as a promising alternative.[22]

In a crystallization process, nucleation is undisputedly the most key factor, which determines the structure, morphology, and size distribution of final products. Nucleants often play a significant role in the enantioselective nucleation through different mechanisms, for example, selectively adsorbing solute molecules from racemic solutions or melts, being adsorbed on nuclei and crystals, and inducing heterogeneous nucleation of specific species.[23] There is no doubt that suitable nucleants can
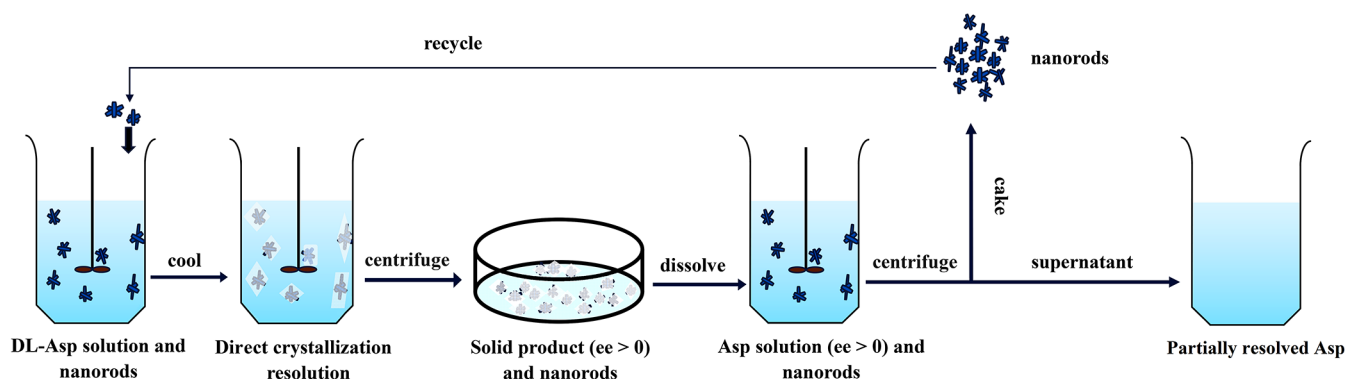
Figure 1. Flowchart of direct crystallization resolution of DL-Asp by chiral nucleants.

intensify the direct crystallization resolution of racemates.[21] To date, nucleants such as insoluble chiral polymers as well as their composites,[24] self-assembly surfaces, etc. have been developed to effectively improve enantioselective crystallization.[25−28] In this work, three optically active nanorods of C_{14}-L-theanine (C_{14}-L-Thea), C_{14}-L-phenylalanine (C_{14}-L-Phe), and C_{14}-D-phenylalanine (C_{14}-D-Phe) were first synthesized by amidation reaction and adequately characterized. Selecting aspartic acid (Asp) as a model chiral system, solid-state characterization as well as solubility measurements were then conducted for D-, L-, and DL-Asp crystals. Meanwhile, the metastable zone widths (MSZWs) as well as the induction periods (t_{ind}) of three species were compared in the absence/ presence of three nanorods as nucleants. The heterogeneous nucleation rates were accordingly obtained by classical heterogeneous nucleation theory (CHNT). After that, the appearance probabilities of enantiomeric and racemic nuclei of Asp from racemate solutions were statistically studied using four supersaturation levels in the absence/presence of chiral nanorods at a nucleation temperature of 303.15 K. Furthermore, under different cooling rates with the addition of 4.0 wt % chiral nanorods of solute mass, the ee values and yields of products from the same racemate solutions were monitored over time. At the same time, the chiral recognition mechanism of the synthesized nanorods to D- and L-Asp was analyzed through quantum mechanics (QM) calculation and molecular dynamics (MD) simulation. Finally, the stability and reusability of three chiral nanorods as heterogeneous nucleants were verified. The direct crystallization resolution of DL-Asp by chiral nucleants in this work was schematically illustrated in Figure 1.

2. CLASSICAL HETEROGENEOUS NUCLEATION THEORY (CHNT)

Based on CHNT, the heterogeneous nucleation rate (J_{het}) in the presence of foreign particles is expressed by[29]

$$J_{het} = B \exp(-\Delta G_{het}^{crit}/\kappa T) \tag{1}$$

where B refers to kinetic constant; T is in Kelvin; κ is Boltzmann constant; and ΔG_{het}^{crit} means the free energy change during the critical nuclei formation in heterogeneous solutions which can be calculated by[30,31]

$$\Delta G_{het}^{crit} = \phi \cdot \Delta G_{hom}^{crit} \tag{2}$$

Here, ϕ stands for the coefficient, and ΔG_{hom}^{crit} means the free energy change during the critical nuclei formation in clear solutions. They are acquired by

$$\phi = \frac{1}{4}(2 + \cos \theta)(1 - \cos \theta)^2 \tag{3}$$

$$\Delta G_{hom}^{crit} = \frac{16\pi\gamma_{hom}^3 V_s^2}{3(\kappa T \ln S)^2} \tag{4}$$

where θ refers to the contact angle of solution on the foreign particles; S is the supersaturation level in practice represented by the ratio of molar fraction concentration (x) to the solubility (x^*) at nucleating temperature; and γ_{hom} refers to the solution−nucleus interfacial energy which can be calculated by[32]

$$\gamma_{hom} = \left(\frac{3\kappa^3 T^3 l}{16\pi V_s^2}\right)^{1/3} \tag{5}$$

Here, V_s is the molecular volume, and l is the slope of $\ln(t_{ind})$ $\sim 1/\ln^2 S$.

In practice, in the presence of foreign particles, the effective interfacial energy (γ_{het}) can be derived from γ_{hom} for a pure homogeneous process as[31]

$$\gamma_{het} = \phi^{1/3} \cdot \gamma_{hom} \tag{6}$$

Furthermore, the radius of critical nuclei (r_{het}^{crit}) as well as the number of molecules in them (n_{het}^{crit}) are calculated by[33,34]

$$r_{het}^{crit} = \frac{2\gamma_{het} V_s}{\kappa T \ln S} \tag{7}$$

$$n_{het}^{crit} = \frac{32\pi\gamma_{het}^3 V_s^2}{3(\kappa T \ln S)^3} \tag{8}$$

The J_{het} can be finally expressed as[29,35]

$$J_{het} = V_s \sqrt{\frac{2\gamma_{het}}{\pi m}} \rho^2 \exp(-\Delta G_{het}^{crit}/\kappa T) \tag{9}$$

Here, m refers to the molecular mass of solute; meanwhile, ρ stands for the number of solute molecules in one volume of nucleating solution.

3. EXPERIMENTAL SECTION

3.1. Materials. D-Aspartic acid (D-Asp, with ee ≥ 99.5%), L-aspartic acid (L-Asp, with ee ≥ 99.5%), DL-aspartic acid (DL-

Asp), D-phenylalanine (D-Phe, with ee ≥ 99.5%), L-phenyl-alanine (L-Phe, with ee ≥ 99.5%), L-theanine acid (L-Thea, with ee ≥ 99.5%), petroleum ether, myristoyl chloride ($C_{14}H_{27}ClO$), acetone, dimethyl sulfoxide (DMSO), NaOH, and HCl were purchased from Adamas-Beta (Shanghai, China). The ee of the received enantiomers and racemate was double checked by HPLC with chiral columns.

3.2. Preparation of Nanorods. Amounts of 4.37 g of L-Thea and 1.00 g of solid-state NaOH were first added into a mixture containing 60 mL of ice water and 40 mL of acetone. Subsequently, excessive myristoyl chloride (7.40 g) was dropped into the mixture at 273.15 K over 1 h under stirring. The stirring was further continued for 2 h after dropping was finished. At the same time, the pH value of the reaction system was kept above 12.0 by the NaOH aqueous solution (1.0 M). The mixture was then acidified to pH = 1.0 with concentrated HCl to precipitate crystalline C_{14}-L-Thea. Finally, the crude crystals were washed using water and petroleum ether, respectively, and dried in a vacuum. C_{14}-L-Phe and C_{14}-D-Phe were also synthesized using the same method.[36]

3.3. Characterization of Nanorods. ^{1}H NMR spectroscopy was performed on an AS600 spectrometer (Q. One Instruments, Wuhan, China) at room temperature. Reported free-induction decay signals were the average of 32 scans. The recycle delay between scans was set as 10 s.[37] IR was carried out using a 650 spectrometer (Gangdong, Tianjin, China). The scanning wavenumber ranged from 500 to 4000 cm^{-1}.[38] PXRD was operated on a TD-3700 diffractometer with Cu Kα radiation (Tongda Instruments, Dandong, China). The step length from 3 to 80° was 0.05°, and the time per step was 5 s.[39] The thermal analyses by DSC and TGA were conducted on an HSC-4 differential scanning calorimeter (Henjiu Experimental Equipment, Bejing, China) and a WRT-12 thermogravimetric analyzer (Beiguang Hongyuan Instruments, Beijing, China), respectively. The heating rate was 5.0 K per minute.[38] DLS was employed for the measurement of particle size distribution using a Zen 3690 nanosizer with an APD detector (Malvern Panalytical, Malvern, UK). A 4 mW helium−neon gas laser was used as the light source (633 nm). The scattering angle range was set from 30 to 90°.[40] The morphologies of the synthesized nanorods were viewed using a Gemini 300 SEM system (Zeiss, Oberkochen, Germany). Before being observed, the samples were coated by gold in advance.[41] The optical rotations of nanorods were measured on an SGW 532 polarimeter (Wuguang Instruments, Shanghai, China) at 589 nm with an accuracy of ±0.001°. The nanorods were dissolved in DMSO before measurements.[42] The contact angles on nanorods of L-, D-, and DL-Asp saturated aqueous solutions at 298.15 K were measured using an SDC-200S contact angle goniometer (Sindin, Dongguan, China) with the measuring angle range and the accuracy of 0 to 180° and ±0.1°, respectively. During measurements, the droplet volume was 1.0 μL, and the temperature was 296.15 K.[43]

3.4. Characterization of Crystalline Enantiomers and Racemates. The solid-state characterization of three species of Asp was carried out by use of IR and PXRD, respectively. The details were described as above.

3.5. Molar Fraction Solubility Measurements. The solubilities of three species of Asp in water from 288.15 to 323.15 K were determined, referring to ref 39. Each solubility measurement was performed using 50 mL of double-jacketed crystallizers. First, excessive solid solutes were transferred into the crystallizers, in which 30 mL of water was preadded. The

suspensions were at desired temperatures and regulated by an HH-S11.6 water bath (Jingda, Changzhou, China) with magnetic stirring for 48 h to attain liquid−solid equilibrium. After that, the suspensions stood for 24 h without stirring. Amounts of 3.0 mL of supernatants were then collected and filtered, and 1.0 mL of filtrate was moved into vials preweighed by an AUW 120D balance (Shimadzu, Shanghai, China) with an accuracy of ±10 μg. At last, the filtrates as well as the vials were weighed and dried in an DHG-9145A oven (Huitai, Shanghai, China) at a vacuum atmosphere and 318.15 K until the mass stayed unchanged. All measurements were duplicated five times, and the reported solubilities were the average values. To check whether the crystalline forms changed or not during the solubility measurement process, PXRD was utilized to analyze the remaining solids.

3.6. Metastable Zone Width Measurement (MSZW). The MSZWs of three species of Asp in water with or without 4.0 wt % of nanorods to solute were measured using a laser method. A series of saturated solutions were first made up to 30 mL at various temperatures under a stirring of 200 rpm. Then they were cooled using an F25-ME circulator (Julabo, Seelbach, Germany) at 0.20 K/min. Finally the temperatures were recorded as the intensity of the transmitted laser decreased steeply. Each measurement was duplicated four times, and thus the reported MSZWs were their averages.

3.7. Induction Period Measurement. For the purpose of further investigating the influence of newly constructed nanorods upon the nucleation of enantiomeric and racemic crystals, the t_{ind} values in water with or without 4.0 wt % of nanorods to solute were measured using the above-mentioned laser method at 303.15 K and seven supersaturation levels. First, 20 mL of saturated solutions of three species were prepared at seven temperatures in the presence and absence of 4.0 wt % of nanorods to solute. Second, the solutions were rapidly moved to 30 mL of crystallizers of which the temperature was kept at 303.15 K accompanied by the start of stirring of 200 rpm. The moment the stirring was started, the time should be recorded as 0. The time was recorded again as the intensity of the transmitted laser decreased steeply. Each measurement was duplicated four times, and thus the reported t_{ind} values were their averages.

3.8. Statistical Analysis of Nucleation Experiments. In our previous work, the competitive nucleation mechanism of the two enantiomers in racemic solutions was elementarily investigated, showing that an actual nucleation environment might allow one enantiomer to nucleate preferentially, and the breakage of chiral symmetry was more pronounced when supersaturation was low.[44] For further verification, 320 batches of nucleation experiments were conducted using DL-Asp aqueous solution with or without 4.0 wt % of nanorods to solute at 303.15 K and four supersaturation levels. As soon as sufficient amounts of nuclei emerged in the solutions, the suspensions were filtered, immediately followed by the fact that the ee's of cakes were measured by using HPLC. Using pure racemic Asp as the standard sample, the uncertainty of HPLC in the actual measurement was found to be 0.98%. The appearance probability (P) of different types of nuclei was statistically calculated by

$$P = F^*/F \tag{10}$$

where F was the total batches of isolated experiments, and F* was counted into the following categories in light of the ee of nuclei: (i) the batch was counted into the case of L-Asp being
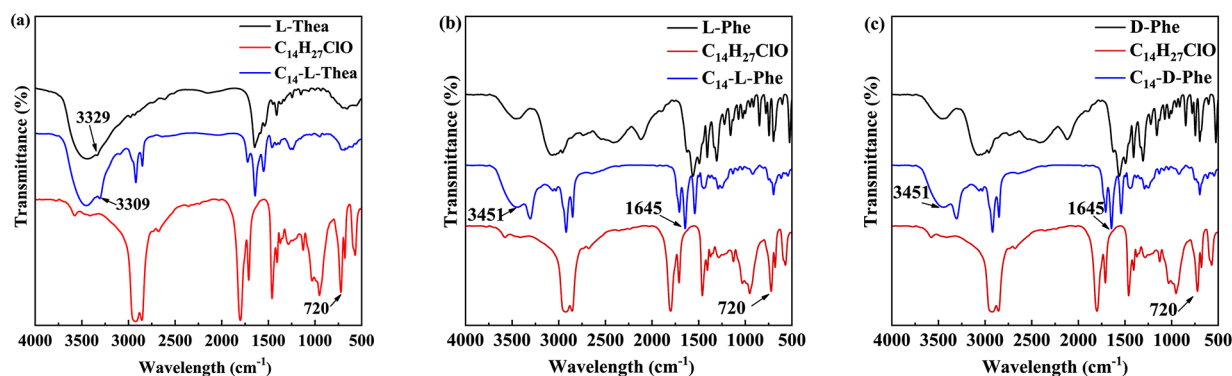
Figure 2. Infrared spectra of L-Thea, myristoyl chloride, and C_{14}-L-Thea (a), L-Phe, myristoyl chloride, and C_{14}-L-Phe (b), and D-Phe, myristoyl chloride, and C_{14}-D-Phe (c).

nucleated if it was larger than 0.98%; (ii) the batch was counted into the case of D-Asp being nucleated if it was less than −0.98%; and (iii) the batch was counted into the case only if DL-Asp was nucleated if it was equal to −0.98% to 0.98%.

3.9. Direct Crystallization Resolution. First, the solutions with a concentration of 1.29×10^{-2} g of DL-Asp/g of H_2O were prepared, filtered, and moved to 500 mL crystallizers, for which the temperature was preset at 318.15 K. After being stirred at 200 rpm for 30 min, the solutions were cooled in the absence and presence of 4.0 wt % of nanorods to solute at 0.025, 0.050, 0.10, and 0.20 K/min, respectively. During the cooling process, the suspensions with or without nanorods were sampled at an interval of 0.5 or 1.0 K; meanwhile, the time as well as the temperature were recorded. Subsequently, the sample suspensions were centrifuged, and the cakes were dried in the oven. The dried solids were dissolved in water, and the mixtures were centrifuged. The cakes were collected, and the ee values of supernatants were measured by use of HPLC. After that, the above experiments were repeated again. Particularly, in the duplicate batches, all suspensions were centrifuged to collect all solids at the times which were determined in the previous batches as the moments the solid maximum ee value emerged, and finally the product yields were calculated by the weight ratio of the precipitated Asp to the feeding Asp.[45]

3.10. Recyclability Examination. After each crystallization resolution experiment, the solid was collected by centrifugation and then dissolved in excess water. The obtained suspension was centrifuged again, and the cake was washed with water and centrifuged twice. The collected nanorods were dried under vacuum and stored in a desiccator for the next crystallization resolution. Meanwhile, the recovered nanorods were recharacterized using the method described in section 3.3.

3.11. HPLC Analysis. The ee values of Asp products from nucleation and crystallization resolution experiments were measured by a LC-20A HPLC system (Shimadzu, Suzhou, China) combined by Crownpak CR(+) series columns (Daicel Chiral Technologies, Shanghai, China) with an uncertainty of 0.98%. An aqueous solution (pH = 1.5) containing 0.27 wt % of perchloric acid was utilized as the mobile phase. The temperature of the column was set at 280.15 K. An UV detector was employed, and it worked at 200 nm.[44]

4. SIMULATION METHODOLOGY

4.1. Quantum Mechanics Calculation. The four structures of D-Asp, L-Asp, C_{14}-L-Thea, and C_{14}-L-Phe were geometrically optimized in water using the Gaussian package at a B3LYP-D3/6-311G** basis set until self-consistency, and the simulation details and results were shown in the Supporting Information (Figures S1 and S2).[46]

4.2. Molecular Dynamics Simulation. In order to further reveal the exact chiral recognition mechanism of chiral nanorods as nucleants, MD simulations were adopted to obtain the structures of the heterogeneous nucleation systems as well as the interactions between C_{14}-L-Thea and two Asp enantiomers. First, eight C_{14}-L-Thea molecules were randomly put into a cylinder box at a length to diameter ratio of 10 in light of the SEM image using the PackMol program to obtain a nanorod model. Then, the model nanorods as well as 100 L-Asp, 100 D-Asp, and 50 000 water molecules were randomly mixed in an $8 \times 8 \times 8$ nm^3 box using Gromacs (ver. 2016.1).[47−51] The number of L-Asp, D-Asp, and water molecules was chosen on the basis of the molar solubility of DL-Asp in water at 318.15 K. Subsequently, the MD simulation was run by energy minimization to remove false interactions and overlaps under periodic boundary conditions. An Amber force field was employed because it could describe small organic compounds made of P, N, O, H, C, as well as halogen.[52] The water model was described by TIP3P. The precise atomic charge in all species was obtained by the Multiwfn program through electrostatic potential fitting. Before quenching, the system was simulated by NVT for 5 ns to equilibrate with 318.15 K and 1.00 atm. During the simulation for the equilibrium, the position of all species except water was restricted. After that, the nucleation state was established by quenching the system to 303.15 K. The quenching time of NPT was set as 15 ns at a step of 2 fs. The system was energetically minimized to build a new equilibrium. Finally, the structure of the nucleating system after new equilibrium was obtained and visually output by use of VMD 1.9. Meanwhile, the interactions between the model nanorod, namely, C_{14}-L-Thea, with L-Asp and D-Asp, respectively, were analyzed through an average independent gradient model (aIGM) also performed on the Multiwfn 3.8 package, and the aIGM isosurface diagrams were displayed by the VMD 1.9. The cutoff distance for such intermolecular interactions of electrostatic and Lennard-Jones was pregiven as 12 Å. The van der Waals force was rectified by the EnerPres option. The long-range electrostatic interaction was obtained

through summation using the particle-mesh Ewald (PME) method. The pressure and temperature were coupled successively by V-rescale and Berendsen algorithms.[53]

5. RESULTS AND DISCUSSION

5.1. Characterization of C_{14}-L-Thea, C_{14}-L-Phe, and C_{14}-D-Phe Nanorods.

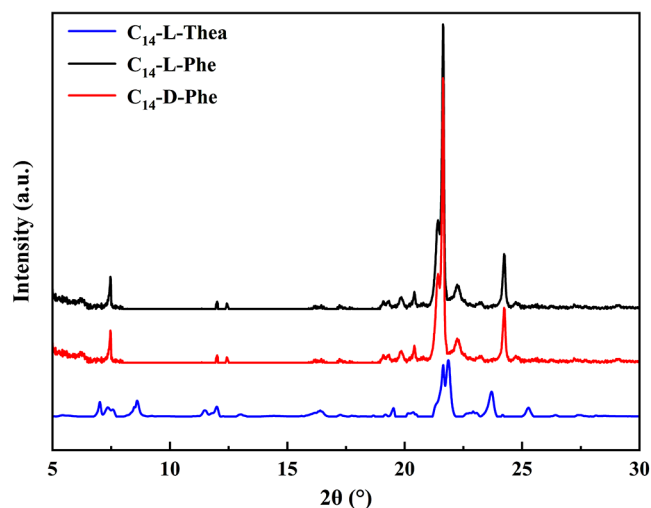The ^1H NMR spectra of three

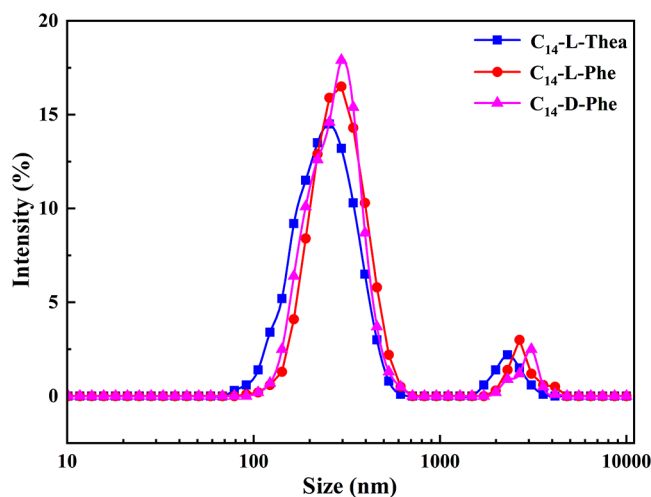**Figure 3.** PXRD patterns of nanorods.

Figure 4. Size distribution curves of C_{14}-L-Thea, C_{14}-L-Phe, and C_{14}-D-Phe.

nanorods are shown in Figure S3 (Supporting Information). The hydrogen protons in the spectrograms can be paired with those of the desired products, indicating that the three nanorods have been successfully synthesized.[37] Meanwhile, the

Table 2. Contact Angles between Nanorods and Solutions

nanorods	contact angles (deg)		
	L-Asp	D-Asp	DL-Asp
C_{14}-L-Thea	101.98	102.67	103.18
C_{14}-L-Phe	123.52	121.45	117.53
C_{14}-D-Phe	124.51	120.96	118.94

Table 3. Solubilities of Three Asp Species in Water

T (K)	$10^3 x^*$		
	L-Asp	D-Asp	DL-Asp
288.15	0.436	0.435	0.667
293.15	0.528	0.525	0.807
298.15	0.636	0.635	0.972
303.15	0.768	0.768	1.155
308.15	0.910	0.909	1.376
313.15	1.091	1.102	1.649
318.15	1.320	1.334	1.931
323.15	1.509	1.523	2.282

yields of C_{14}-L-Thea, C_{14}-L-Phe, and C_{14}-D-Phe are 66.51%, 60.50%, and 64.45%, respectively.

The IR spectra of D-Phe, L-Phe, L-Thea, C_{14}-D-Phe, C_{14}-L-Phe, and C_{14}-L-Thea and myristoyl chloride are presented in Figure 2, respectively. In Figure 2a, the peak around 720 cm^{-1} intimately connected with Cl−C stretching in the acyl halide group of myristoyl chloride is not found in the spectrum of C_{14}-L-Thea, which confirms that Cl has been replaced or removed during the reaction between myristoyl chloride and L-Thea. Besides, the peak around 3329 cm^{-1} that was intimately connected with H−N stretching in the amino group of L-Thea bathochromically shifts to ca. 3309 cm^{-1} in the spectrum of C_{14}-L-Thea, implying C_{14}-L-Thea has been synthesized. As shown in Figure 2b, the peaks around 3451 cm^{-1} as well as 1645 cm^{-1} intimately connected with H−N and C=O stretching, respectively, in the amide group arise in the spectrum of C_{14}-L-Phe, and the peak around 720 cm^{-1} intimately connected with Cl−C stretching in the acyl halide group of myristoyl chloride is not found in the spectrum of C_{14}-L-Phe, which strongly proves that the C_{14}-L-Phe has been successfully prepared. Similarly, as shown in Figure 2c, C_{14}-D-Phe has been synthesized successfully, which has an identical IR spectrum to that of C_{14}-L-Phe.[54]

The PXRD diffractograms of three nanorods from 10° to 35° (2θ) are illustrated in Figure 3. The nanorod of C_{14}-L-Thea possesses such characteristic peaks at ca. 8.6°, 23.7°, 25.2°, etc. The nanorods of C_{14}-D-Phe and C_{14}-L-Phe have identical diffractograms with characteristic peaks at ca. 7.4°, 21.6°, 22.2°, 24.2°, etc. All synthesized nanorods possess a complete crystal structure. Besides, the thermal analyses of nanorods show that the melting points of C_{14}-L-Thea, C_{14}-D-Phe, and

Table 1. Specific Optical Rotation Values of Nanorods in DMSO at 293.15 K

nanorods	$[\alpha]_D^{20}$							
	1	2	3	4	5	6	average	R^a
C_{14}-L-Thea	−2.64	−2.64	−2.64	−2.64	−2.67	−2.67	−2.65	0.015
C_{14}-L-Phe	−18.79	−18.66	−18.39	−17.97	−17.66	−17.28	−18.13	0.594
C_{14}-D-Phe	18.50	18.50	18.20	18.50	18.50	18.20	18.40	0.154

$^a R$ is the standard deviation.
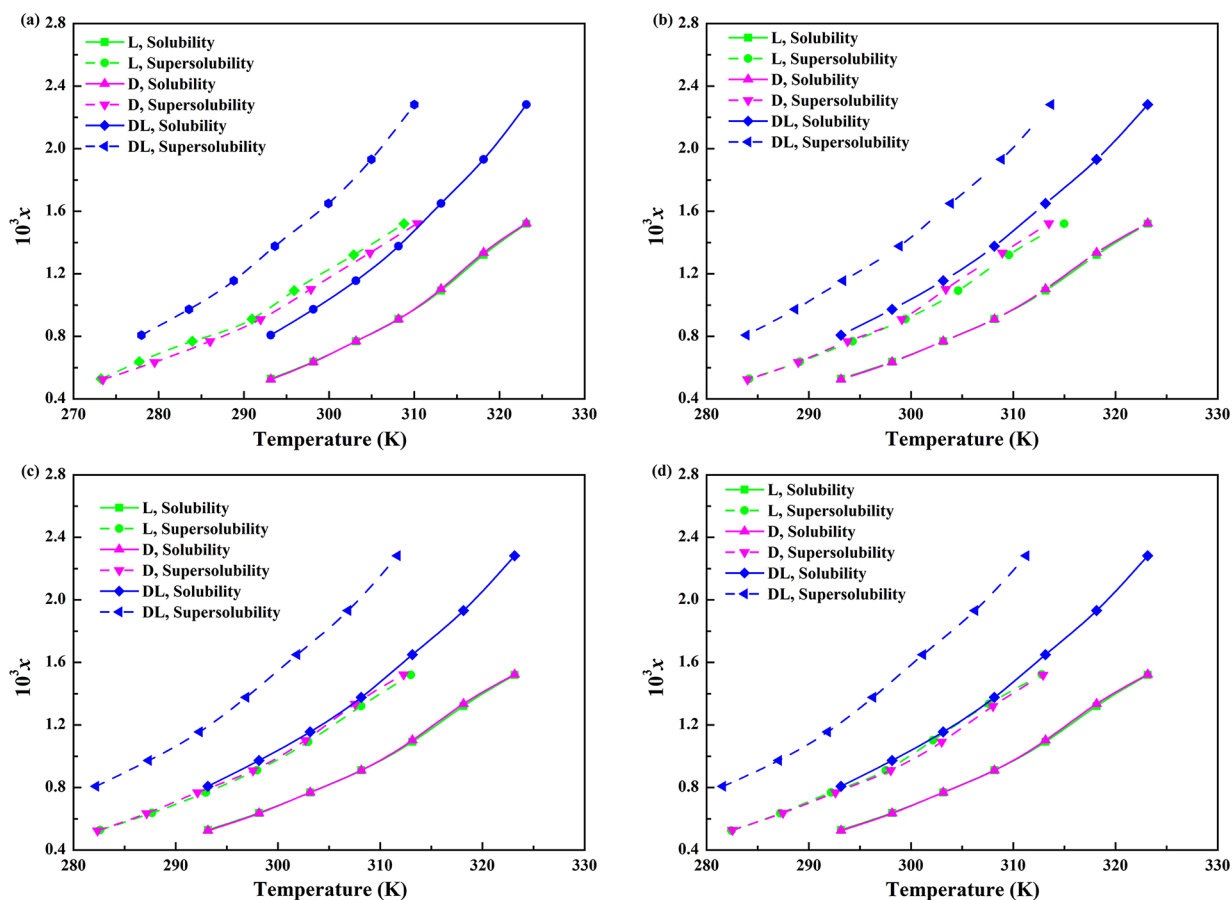
Figure 5. MSZWs of three Asp chiral species in water (a), with C_{14}-L-Thea (b), C_{14}-L-Phe (c), and C_{14}-D-Phe (d).

C_{14}-L-Phe are 390.41, 340.13, and 338.75 K, respectively (Figure S4, Supporting Information).

The SEM images of C_{14}-L-Thea, C_{14}-D-Phe, and C_{14}-L-Phe nanorods in Figure S5 (Supporting Information) show that they are rod-like, and their size distribution curves are illustrated in Figure 4. Each nanorod with a certain aspect ratio exhibits two peaks with average hydrodynamic diameters of 252.46−294.66 nm and 2.36−2.89 μm, respectively. The former and latter peaks might be associated with the diameter and length of the nanorods, respectively, as their agglomeration can be ignored. Meanwhile, the polydispersity indexes (PDIs) derived from two peaks of three nanorods are 0.10−0.13 and 0.02−0.04, respectively, implying that the three as-prepared nanorods possess uniform sizes.[40]

The specific optical rotations of C_{14}-L-Thea, C_{14}-D-Phe, and C_{14}-L-Phe nanorods in DMSO at 293.15 K are listed in Table 1. The concentration of the solution used to calculate the specific rotation is 4 mg/mL. The average specific optical rotations of the three nanorods are −2.65, −18.13, and 18.40, respectively.[42]

The contact angles of L-, D-, and DL-Asp saturated aqueous solutions at 298.15 K on the nanorods are listed in Table 2, which are acquired from the snapshots supplemented in the Supporting Information as Figure S6. All three nanorods exhibit hydrophobicity in which C_{14}-D-Phe is the most hydrophobic with maximum L-Asp, D-Asp, and DL-Asp contact angles of 124.51°, 120.96°, and 118.94°, respectively, whereas C_{14}-L-Thea is the least hydrophobic with those of 101.98°, 102.67°, and 103.18°, respectively. In theory, C_{14}-L-Phe and

C_{14}-D-Phe are enantiomers, and the contact angles of DL-Asp solutions on them should be the same. In practice, the contact angles should also be related to the morphology and size of particles, which leads to the deviation. Furthermore, the difference in hydrophobicity of three nanorods is certainly related to the fact that different functional groups exist on their surfaces.[43]

5.2. Chiral Nature of Studied Model Systems. The IR and PXRD spectrograms of enantiomeric and racemic Asp crystals are presented in Figure S7 (Supporting Information), which are consistent with those reported by Lee et al.[55] and Pinto et al.[56]

The solubilities of three species in water are shown in Table 3, which is in accordance with the work of Wu et al.[57] All three substances possess positive solubility characteristics, but in general under the same temperature the solubility of DL-Asp is about 1.5 times larger than those of L-Asp and D-Asp, which are the same. In addition, by comparing the PXRD patterns of solid residuals after equilibrium with those of raw materials (Figure S8, Supporting Information), there is no crystalline form change in the solubility measurement.

The early identification of its racemic nature of a racemate is extremely vital for the selection and design of its practical crystallization resolution. The IR spectra, PXRD diffractograms, and molar fraction solubilities of three species of Asp illustrate that the chiral nature of DL-Asp belongs to a racemic compound, which is in accordance with the work of Lee and Lin who have reported the ee value at one of the eutectic points of the racemic system to be ca. 67%.[55]
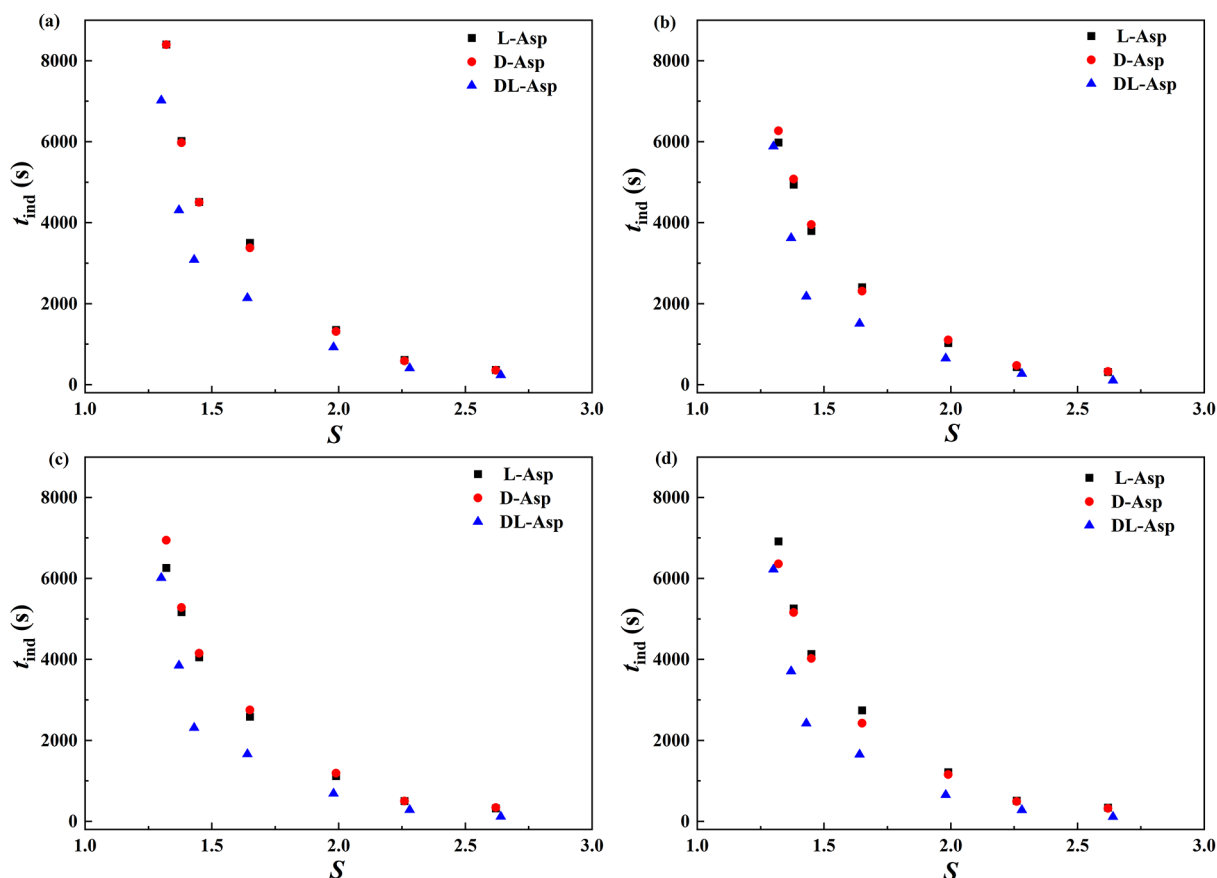
Figure 6. Influence of S on the t_{ind} of Asp in water (a), with C_{14}-L-Thea (b), C_{14}-L-Phe (c), and C_{14}-D-Phe (d) at 303.15 K.
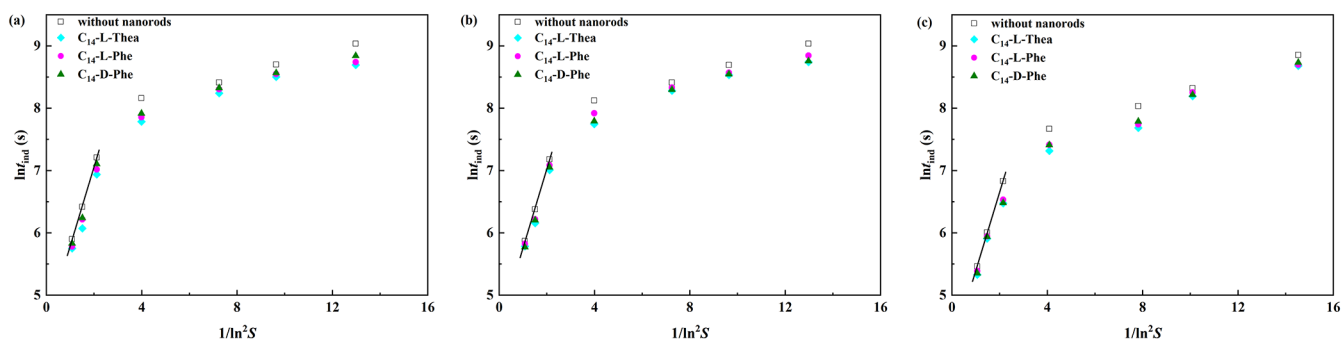
Figure 7. Plots of t_{ind} versus S in the absence/presence of nanorods: L-Asp (a), D-Asp (b), and DL-Asp (c).

5.3. Metastable Zone Widths. Figure 5 depicts a series of MSZWs of three species of Asp in water with or without 4.0 wt % of nanorods to solute. In the pure water, when being cooled from the same saturation temperature and at the same cooling rate, the average MSZWs are 17.56 K for L-Asp, 16.14 K for D-Asp, and 13.99 K for DL-Asp, respectively (Figure 5a). Correspondingly, they decrease to 8.67, 9.34, and 9.46 K in the presence of C_{14}-L-Thea (Figure 5b) and to 10.26, 10.76, and 11.12 K in the presence of C_{14}-L-Phe (Figure 5c), respectively. Similarly, as shown in Figure 5d, when C_{14}-D-Phe is added, they decrease to 10.73, 10.36, and 11.58 K, respectively.

In general, the average MSZWs of three species become narrow when the nanorods are added as nucleants.[58] The nucleation barrier of Asp species is reduced, and the solute molecules are easier to nucleate in the presence of nanorods. In

particular, the average MSZWs of L-Asp become narrower than those of D-Asp when using L-nanorods as nucleants, and vice versa. That is, the chiral nanorods can mostly promote the nucleation of those enantiomeric crystals having an identical chirality to the rods', which shall provide more opportunities to acquire pure enantiomeric crystals when using them as nucleation promoters. Furthermore, the promotion degree by C_{14}-L-Thea to the nucleation of L-Asp is larger than that by C_{14}-L-Phe, which contributes to a smaller contact angle of L-Asp solution on the former surface, leading to a smaller nucleation barrier than C_{14}-L-Phe.

5.4. Induction Period. As shown in Figure 6 and Table S1 (Supporting Information), the t_{ind} values of three chiral species generally decrease with increasing S, and in the absence of nanorods, under the same S, the t_{ind} values of enantiomeric crystals are almost the same but larger than that of racemic

Table 4. Heterogeneous Nucleation Parameters at 303.15 K by Using the Nanorods

| nucleant	crystal	ϕ	S	ΔG_{hom}^{crit} (J)	ΔG_{het}^{crit} (J)	n_{het}^{crit}	r_{het}^{crit} (nm)	γ_{het} (J/m^2)	j_{het} (#/(m^3·s))
C$_{14}$-L-Thea	L-Asp	0.653	1.99	7.72×10^{-21}	5.04×10^{-21}	5.09	0.543	0.00593	1.77×10^{23}
			2.26	6.52×10^{-21}	4.26×10^{-21}	3.06	0.458		3.01×10^{23}
			2.62	5.52×10^{-21}	3.60×10^{-21}	1.86	0.388		4.78×10^{23}
	D-Asp	0.662	1.99	7.72×10^{-21}	5.11×10^{-21}	5.16	0.546	0.00596	1.74×10^{23}
			2.26	6.52×10^{-21}	4.31×10^{-21}	3.10	0.460		2.97×10^{23}
			2.62	5.52×10^{-21}	3.65×10^{-21}	1.88	0.390		4.73×10^{23}
	DL-Asp	0.668	1.98	7.71×10^{-21}	5.15×10^{-21}	5.28	0.553	0.00589	3.92×10^{23}
			2.28	6.39×10^{-21}	4.27×10^{-21}	3.00	0.458		6.48×10^{23}
			2.64	5.43×10^{-21}	3.62×10^{-21}	1.84	0.389		1.01×10^{24}
C$_{14}$-L-Phe	L-Asp	0.872	1.99	7.72×10^{-21}	6.73×10^{-21}	6.78	0.598	0.00653	1.24×10^{23}
			2.26	6.52×10^{-21}	5.68×10^{-21}	4.09	0.505		2.25×10^{23}
			2.62	5.52×10^{-21}	4.81×10^{-21}	2.48	0.427		3.76×10^{23}
	D-Asp	0.856	1.99	7.72×10^{-21}	6.61×10^{-21}	6.67	0.594	0.00649	1.27×10^{23}
			2.26	6.52×10^{-21}	5.58×10^{-21}	4.01	0.502		2.29×10^{23}
			2.62	5.52×10^{-21}	4.72×10^{-21}	2.43	0.425		3.82×10^{23}
	DL-Asp	0.897	1.98	7.71×10^{-21}	6.92×10^{-21}	7.09	0.610	0.00649	2.70×10^{23}
			2.28	6.39×10^{-21}	5.73×10^{-21}	4.03	0.506		4.80×10^{23}
			2.64	5.43×10^{-21}	4.87×10^{-21}	2.47	0.429		7.91×10^{23}
C$_{14}$-D-Phe	L-Asp	0.879	1.99	7.72×10^{-21}	6.79×10^{-21}	6.85	0.600	0.00655	1.22×10^{23}
			2.26	6.52×10^{-21}	5.73×10^{-21}	4.12	0.506		2.22×10^{23}
			2.62	5.52×10^{-21}	4.85×10^{-21}	2.50	0.428		3.73×10^{23}
	D-Asp	0.852	1.99	7.72×10^{-21}	6.58×10^{-21}	6.64	0.594	0.00648	1.28×10^{23}
			2.26	6.52×10^{-21}	5.55×10^{-21}	3.99	0.501		2.31×10^{23}
			2.62	5.52×10^{-21}	4.70×10^{-21}	2.42	0.424		3.84×10^{23}
	DL-Asp	0.835	1.98	7.71×10^{-21}	6.44×10^{-21}	6.59	0.596	0.00634	3.00×10^{23}
			2.28	6.39×10^{-21}	5.33×10^{-21}	3.75	0.494		5.21×10^{23}
			2.64	5.43×10^{-21}	4.53×10^{-21}	2.30	0.419		8.47×10^{23}
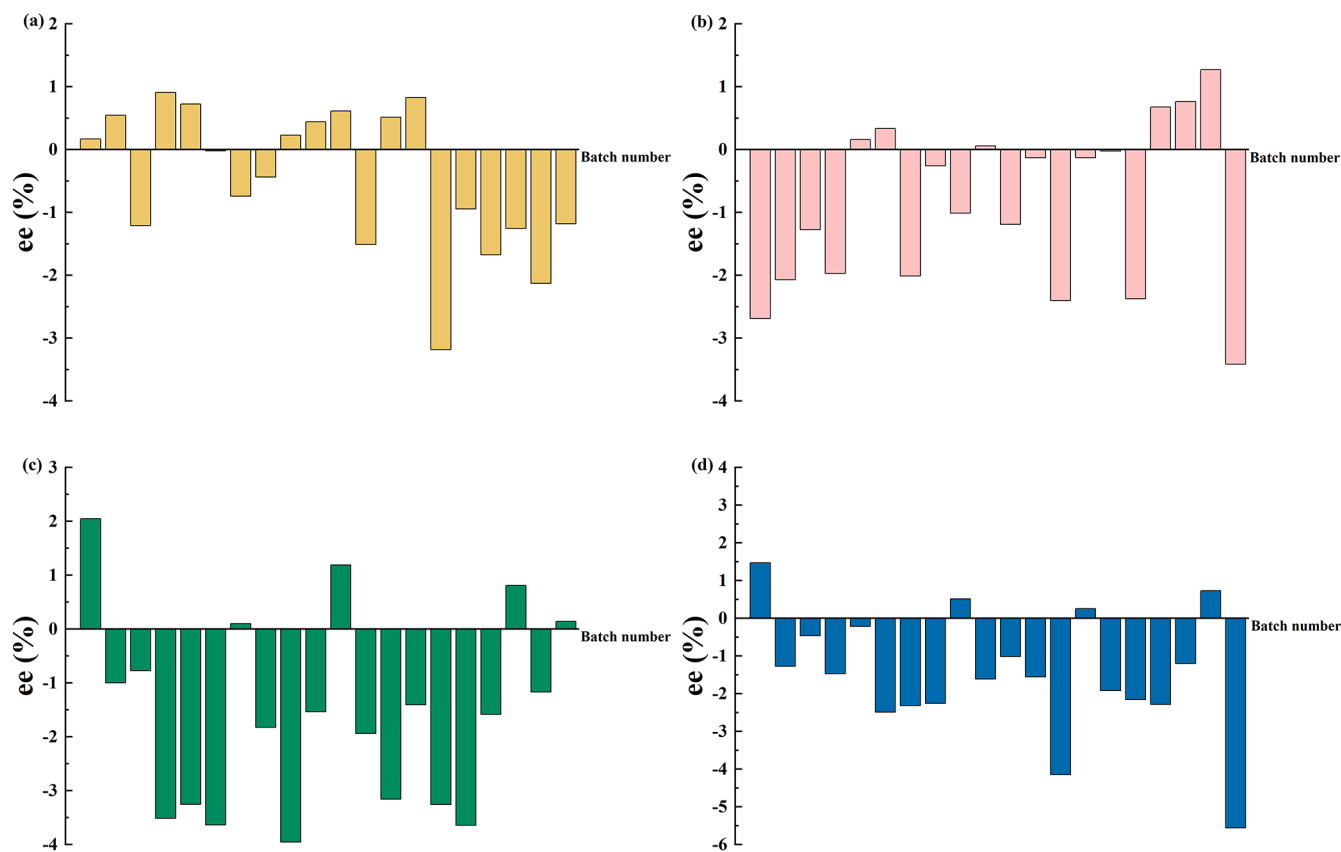
Figure 8. ee of initial particles collected from homogeneous nucleation experiments at different S: 1.67 (a), 1.43 (b), 1.19 (c), and 1.08 (d).
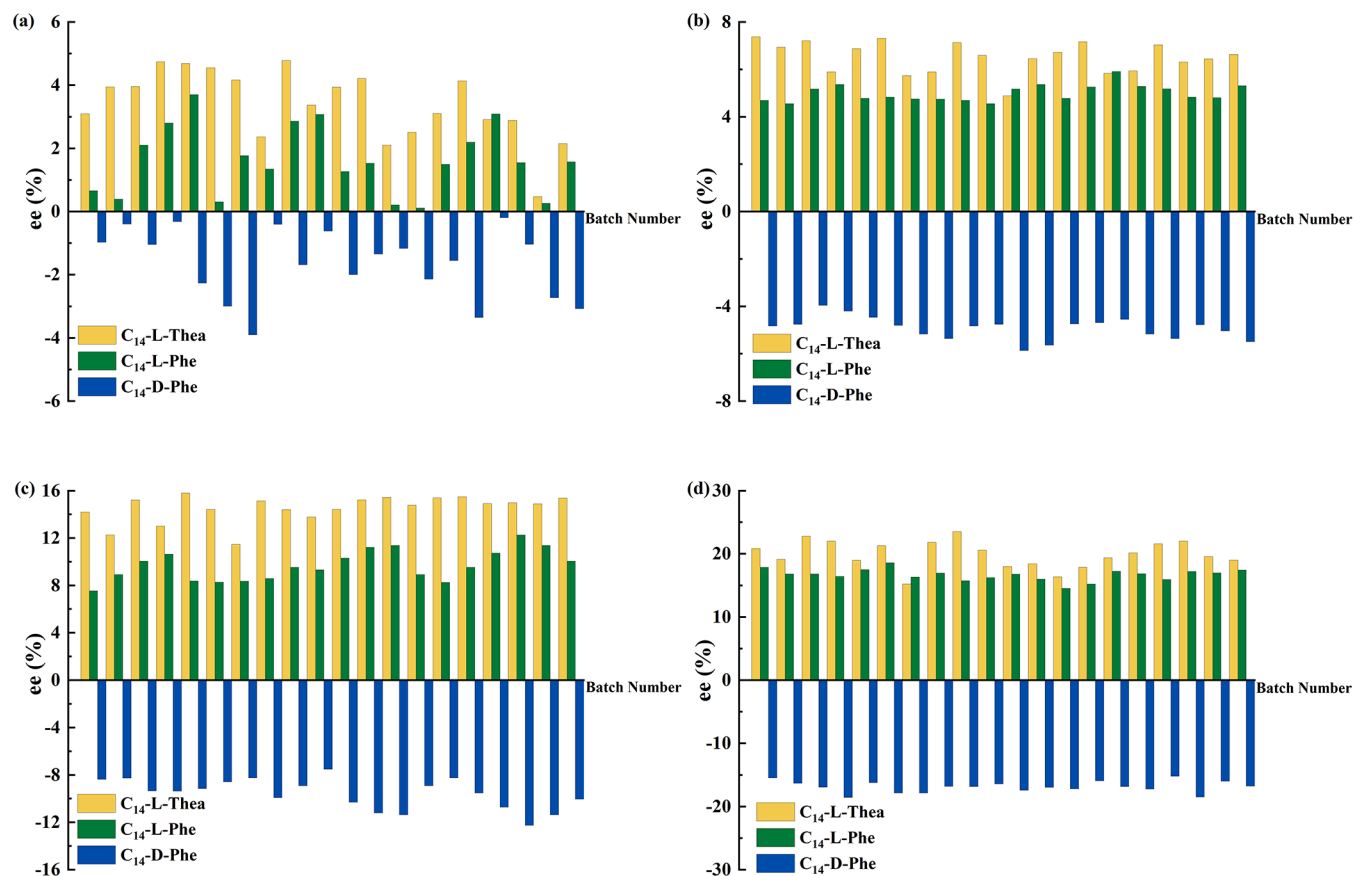
Figure 9. ee of initial particles collected from heterogeneous nucleation experiments at different S: 1.67 (a), 1.43 (b), 1.19 (c), and 1.08 (d).

crystals; that is, DL-Asp has the narrowest MSZW and the shortest t_{ind}.

In addition, in the presence of nanorods, the t_{ind} values of all species are shortened. At each S, the t_{ind} order is D- > L- > DL-Asp when C_{14}-L-Thea and C_{14}-L-Phe are presented, suggesting that L-nanorods are more promotive to the nucleation of L-crystals than that of D-crystals. Likewise, when C_{14}-D-Phe is presented, the order of t_{ind} changes to L- > D- > DL-Asp, indicating that D-nanorods are more promotive on the nucleation of D-crystals than that of L-crystals. The results are in accordance with those of MSZW measurements.[59]

5.5. Heterogeneous Nucleation Rates. To further study the effect of three as-prepared chiral nanorods on the nucleation of various Asp crystals, their primary nucleation parameters in the absence/presence of the chiral nanorods have been obtained using CHNT. The scatter plots of $\ln(t_{ind})$ over $1/\ln^2 S$ in the absence/presence of nanorods are illustrated in Figure 7. It is obvious that when t_{ind} is measured in the pure water with high supersaturation, the scatter plots of $\ln(t_{ind})$ over $1/\ln^2 S$ can be well fitted into a straight line to obtain the slope. Nevertheless, when the supersaturation is at low levels or in the presence of nanorods, the scatter plots of $\ln(t_{ind})$ over $1/\ln^2 S$ are incapable of being fitted into straight lines because in this case the measured t_{ind} values are generally inaccurate. In this work, the heterogeneous nucleation rates in the presence of nanorods have been calculated using eqs 1−9. Table 4 lists the heterogeneous nucleation parameters at 303.15 K and different S values.

At each S without nanorods, the nucleation rates of L- and D-crystals are nearly equal, and both are less than that of DL-

crystals. In the case that the nanorods are presented, the ΔG_{het}^{crit} of the three crystals decreases, resulting in increased nucleation rates which increase with S. However, different nanorods have different degrees of change in the nucleation rates of the three crystals. When C_{14}-L-Phe or C_{14}-D-Phe is added, the nucleation rate order of L-, D-, and DL-Asp crystals from their respective supersaturated solutions is DL- > D- > L-Asp. However, when C_{14}-L-Thea is added, the order becomes DL- > L- > D-Asp. Moreover, when C_{14}-L-Thea is used as the nucleant, the nucleation rates of enantiomeric and racemic crystals are higher than those using the other two nucleants. It might be because the hydrophilicity of C_{14}-L-Thea to L-, D-, and DL-Asp solutions is the highest, leading to it having the most promotion on nucleation.

5.6. Statistical Analyses. The statistical results on the homogeneous nucleation in the racemate solutions at different S are shown in Figure 8 and Table S2 (Supporting Information). At S values of 1.67, 1.43, 1.19, and 1.08, the P of the L-enantiomeric nuclei is 0%, 5%, 10%, and 5%, respectively, and that of the D-enantiomeric nuclei is 35%, 50%, 65%, and 70%, respectively. Besides, the P of the racemic nuclei is 65%, 45%, 25%, and 25%, respectively. In the initial precipitates, the amount of DL-Asp is far greater than that of D-Asp or L-Asp, resulting in very low ee values of the collected solids. Generally, the nucleation of enantiomeric crystals accompanied by the appearance of racemic nuclei remains highly random. In addition, by comparing the nucleation probabilities under the four S, it is found that S has some effect on the P, and the influence law is the same as the results of our previous work.[44] That is, the appearance probability of D-
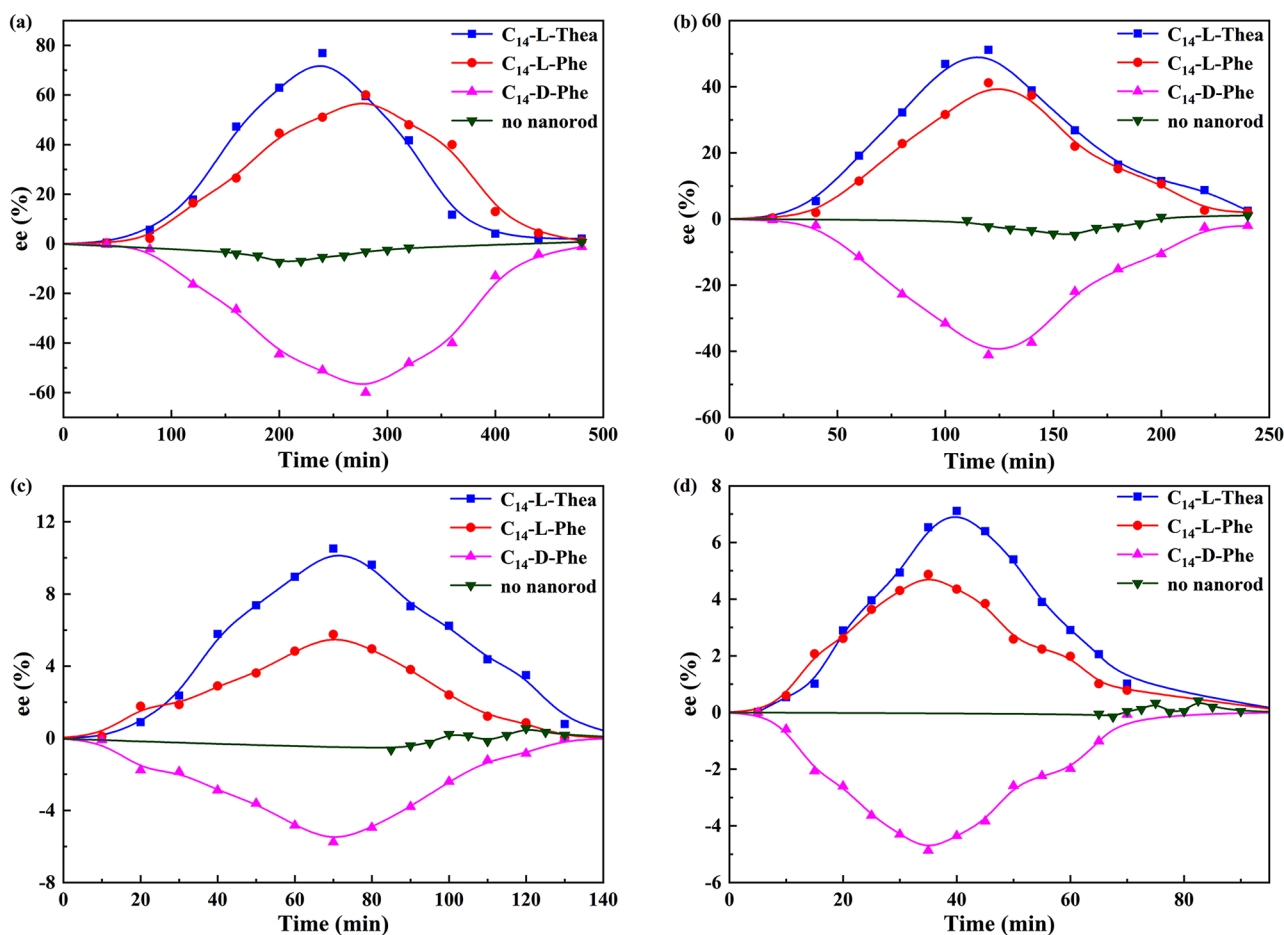
Figure 10. ee of solid products over time at cooling rates of 0.025 (a), 0.05 (b), 0.10 (c), and 0.20 K/min (d).
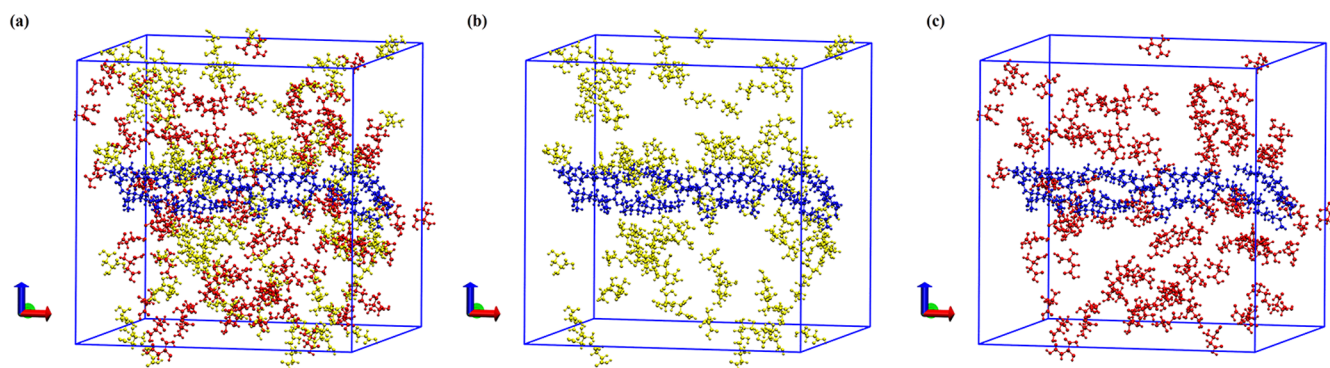

Figure 11. Snapshots in the final state of C_{14}-L-Thea, L-Asp, and D-Asp (a), C_{14}-L-Thea and L-Asp (b), and C_{14}-L-Thea and D-Asp (c) in the nucleating system.

enantiomeric nuclei increases with the decline of *S*, and vice versa.

The statistical results on the heterogeneous nucleation in the racemate solutions with nanorods at different *S* are shown in Figure 9 and Table S3 (Supporting Information). When nanorods are presented, the diversity vanishes, and *P* increases to 100% at low *S*. Specifically, when L-nanorods are added, the nucleation of L-Asp crystals is completely promoted, and the D-nanorod has the same promoted to D-Asp crystals. In addition, the ee value of nucleation products increases significantly with the decline of *S*. This may be because at low *S* the smaller the nucleation driving force is, the slower the nucleation rate

becomes, the longer the time is for the chiral recognition, and the higher the optical purity of the nuclei achieved. Specifically, at the same *S*, when C_{14}-L-Phe is added, L-Asp is induced to preferentially nucleate, and D-Asp is also preferentially nucleated when C_{14}-D-Phe is used. By comparing the statistical results of those using C_{14}-L-Thea and C_{14}-L-Phe, the ee value of nuclei induced by C_{14}-L-Thea is generally larger than that by C_{14}-L-Phe. It is probably because C_{14}-L-Thea has an additional amide (CONH) group compared to C_{14}-L-Phe, which provides more hydrogen-bond acceptors and donors to intensify the intermolecular interaction between C_{14}-L-Thea and L-Asp, resulting in a higher chiral recognition ability.[60]
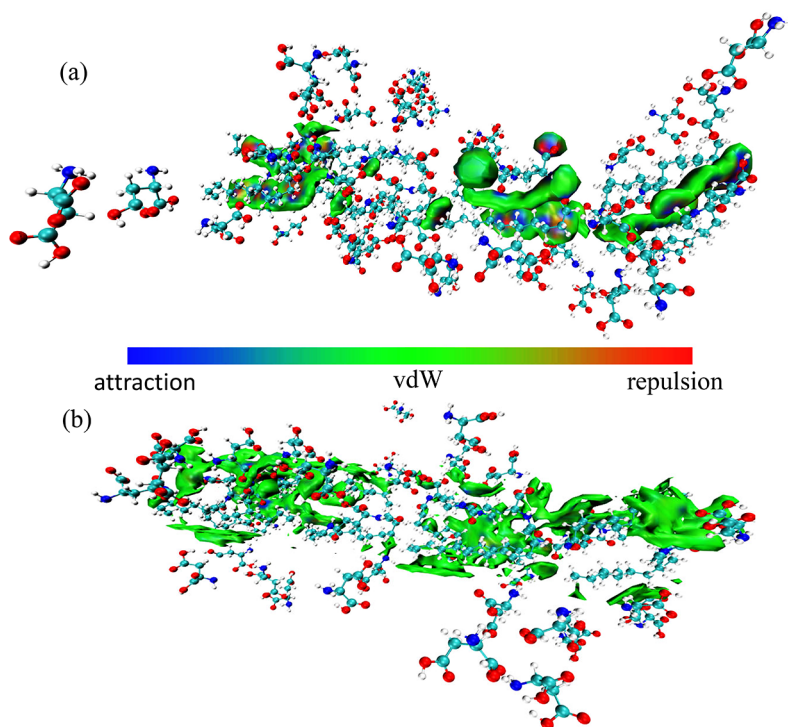
Figure 12. AIGM isosurface diagrams of C_{14}-L-Thea with L-Asp (a) and C_{14}-L-Thea with D-Asp (b). The isosurface of aIGM = 0.1.
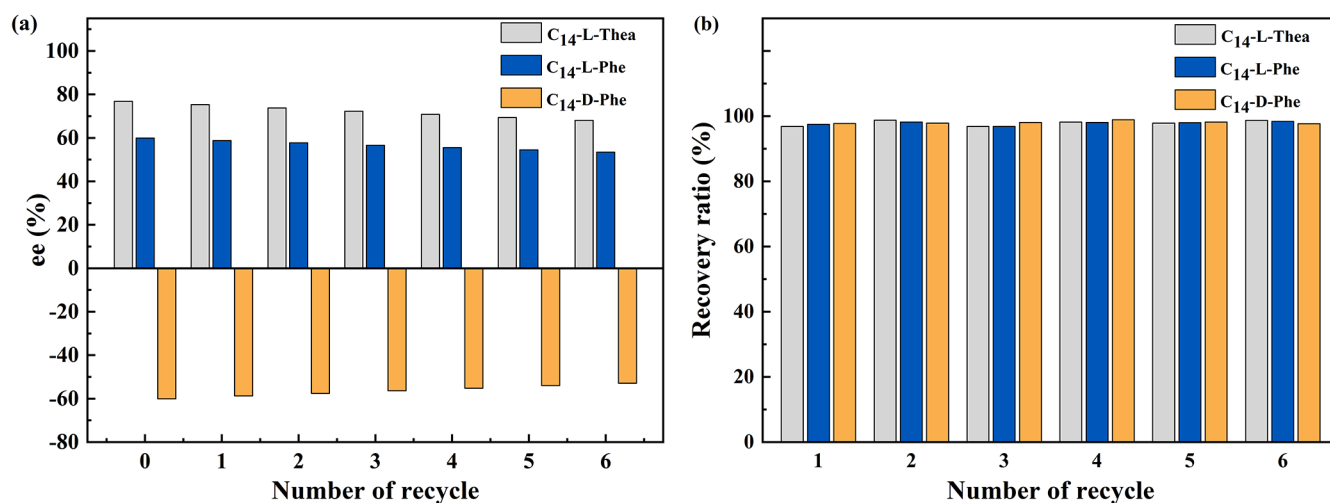

Figure 13. Effect of cycle number on the ee values of products using recovered nanorods (a) and their recovery ratios (b).

5.7. Direct Crystallization Resolution. The ee values of solids over time crystallized from DL-Asp aqueous solutions with or without three nanorods at four cooling rates are shown in Figure 10, and the raw data of ee values as well as the yields are listed in Tables S4, S5, S6, S7, and S8 (Supporting Information), respectively. At all used cooling rates, when DL-Asp solutions are cooled without nanorods, spontaneous crystallization can not resolve or even partially resolve the racemic Asp. While DL-Asp solutions are cooled with nanorods, all ee values are significantly increased. In particular, the ee values of products first rise and then fall with time under different cooling rates. In the first stage, the added chiral nanorods act as nucleation centers with enantioselectivity, and the adsorbed enantiomers accordingly become seeds, resulting in the increase in the ee value of the product. When the

nucleated DL-crystals are much more than enantiomeric crystals, the ee value starts to decrease and finally is close to zero at the completion of crystallization.[21]

Besides, the ee value of the product from a direct crystallization resolution with C_{14}-L-Thea is larger than that with C_{14}-L-Phe, which is certainly because the former has a higher enantioselective capability than the latter.[61] Meanwhile, it is also observed that the slower the cooling rate employed, the higher the ee value of the product achieved. This may be because the slower the cooling rate adopted, the smaller the nucleation driving force becomes, which is beneficial to the nucleation of the enantiomeric crystals having an identical chirality to the rods. When the cooling rate is 0.025 K/min and C_{14}-L-Thea is used as the nucleant, a solid product containing

mainly L-Asp with a maximum ee of 76.85% and a yield of 14.41% is directly crystallized from DL-Asp solutions.

5.8. Molecular Dynamics Simulation. A snapshot of all molecules with water in the nucleating system in the final state simulated by MD is shown in Figure 11a, and blue, yellow, and red molecules refer to C_{14}-L-Thea, L-Asp, and D-Asp, respectively. In order to exhibit the aggregation state between C_{14}-L-Thea and L-Asp or D-Asp more intuitively, C_{14}-L-Thea and L-Asp or D-Asp are extracted and shown in Figure 11b and 11c, respectively. By comparing Figures 11b with 11c, the C_{14}-L-Thea is slightly closer to L-Asp than to D-Asp, showing that the interactions between C_{14}-L-Thea and L-Asp may be larger than those between C_{14}-L-Thea and D-Asp.

The average weak interactions based on MD simulations can provide much more accurate and smoother isosurfaces of C_{14}-L-Thea with L-Asp or D-Asp than that on QM calculations (Figure S2, Supporting Information).[62] The aIGM isosurface diagrams are shown in Figure 12 in which van der Waals interaction, steric repulsion, as well as hydrogen bonding are in green, blue, and red, respectively. In particular, compared with Figure 12b, more blue domains emerge in Figure 12a, diagrammatically presenting that stronger interactions exist between C_{14}-L-Thea and L-Asp than C_{14}-L-Thea and D-Asp.

5.9. Recyclability Examination. The reusability of the nanorods can be evaluated by their recovery ratios after each direct crystallization resolution experiment and the ee values of products using the recovered nanorods as nucleants. As shown in Figure 13, the ee values of products declined from 10.9% to 12.0% after six cycles, and the average recovery ratios of nanoroads are around 97.7% per cycle, which confirms that the nanorods have good reusability. In addition, the ee values of products decline after six cycles, which may be due to the adsorption of impurities on the nanorods. Meanwhile, the morphologies and diffractograms of the recovered nanorods after six cycles recharacterized by PXRD and SEM, respectively (Figures S9 and S10, Supporting Information), are consistent with those of the fresh ones, further proving that the nanorods can keep stable during the direct crystallization resolution operation.[63]

6. CONCLUSIONS

In this work, three optically active nanorods of C_{14}-L-Thea, C_{14}-L-Phe, and C_{14}-D-Phe have been synthesized and used for the direct crystallization resolution of DL-Asp as nucleants. The nucleation experiments and their statistical analysis show that the synthesized chiral nanorods could affect the nucleation parameters and rates of the three species of Asp to a certain extent. In particular, the chiral nanorods can mostly promote the nucleation of enantiomeric crystals with the same chirality and inhibit that of those with opposite chirality to them. The simulation results reveal that a higher chiral recognition of C_{14}-L-Thea than C_{14}-L-Phe to Asp enantiomers is because the difference in hydrogen bonding between C_{14}-L-Thea and Asp enantiomers is larger than that between C_{14}-L-Phe and Asp enantiomers. When 4.0 wt % of C_{14}-L-Thea to solute is added, the ee value of the product crystallized from the DL-Asp solution can be up to 76.85% with a yield of 14.41% under slow cooling. Moreover, the constructed nanorods exhibit good stability and recyclability. The research demonstrates that the chiral nanorods can enhance the direct crystallization resolution of racemic compounds when they are used as the nucleants.

■ ASSOCIATED CONTENT

ⓈI Supporting Information

The Supporting Information is available free of charge at https://pubs.org/doi/10.1021/acsomega.2c01596.

Simulation details and results of QM (Figure S1 and S2); ^{1}H NMR spectra of nanorods (Figure S3); thermal analyses of nanorods (Figure S4); SEM images of nanorods (Figure S5); snapshots of contact angle measurements (Figure S6); IR and PXRD spectra of enantiomeric and racemic Asp crystals (Figure S7); raw data of t_{ind} at 303.15 K (Table S1); raw data of the ee of initial particles collected from homogeneous nucleation (Table S2); raw data of the ee of initial particles collected from heterogeneous nucleation (Table S3); raw data of the ee of solid products over time (Tables S4−S7); yield of Asp at the moments the solid maximum ee value emerged (Table S8); PXRD patterns of raw crystals and residual solids after solid−liquid equilibria (Figure S8); PXRD patterns of raw and recycled nanorods (Figure S9); and SEM images of recycled nanorods (Figure S10) (PDF)

■ AUTHOR INFORMATION

Corresponding Author

Jie Lu − *Chemical Engineering Department, Frontier Medical Technologies Institute, Shanghai University of Engineering Science, Shanghai 201620, China;* ⓞ orcid.org/0000-0002-4581-2032; Phone: +86 21 6779 1216; Email: lujie@sues.edu.cn; Fax: +86 21 6779 1214

Authors

Jiaojiao Cao − *Chemical Engineering Department, Frontier Medical Technologies Institute, Shanghai University of Engineering Science, Shanghai 201620, China*

Boxuan Lou − *Chemical Engineering Department, Frontier Medical Technologies Institute, Shanghai University of Engineering Science, Shanghai 201620, China*

Yue Xu − *Chemical Engineering Department, Frontier Medical Technologies Institute, Shanghai University of Engineering Science, Shanghai 201620, China*

Xiaolan Qin − *Chemical Engineering Department, Frontier Medical Technologies Institute, Shanghai University of Engineering Science, Shanghai 201620, China*

Haikuan Yuan − *Chemical Engineering Department, Frontier Medical Technologies Institute, Shanghai University of Engineering Science, Shanghai 201620, China*

Lijuan Zhang − *Chemical Engineering Department, Frontier Medical Technologies Institute, Shanghai University of Engineering Science, Shanghai 201620, China*

Yan Zhang − *Department of Process Engineering, Memorial University of Newfoundland, St John's NL A1B 3X5, Canada;* ⓞ orcid.org/0000-0003-0107-1014

Sohrab Rohani − *Department of Chemical and Biochemical Engineering, Western University, London N6A 5B9, Canada;* ⓞ orcid.org/0000-0002-1667-1736

Complete contact information is available at:
https://pubs.org/10.1021/acsomega.2c01596

Author Contributions

||J.C., B.L., and Y.X. contributed equally to this work. Jiaojiao Cao: Methodology, Experimental. Boxuan Lou: Data analysis. Yue Xu, Xiaolan Qin: Writing - original draft. Haikuan Yuan:

■ REFERENCES

(1) Aloni, S. S.; Perovic, M.; Weitman, M.; Cohen, R.; Oschatz, M.; Mastai, Y. Amino acid-based ionic liquids as precursors for the synthesis of chiral nanoporous carbons. *Nanoscale Adv.* **2019**, *1*, 4981−4988.

(2) Mastai, Y. Enantioselective crystallization on nanochiral surfaces. *Chem. Soc. Rev.* **2009**, *38*, 772−780.

(3) Ward, T. J.; Baker, B. A. Chiral separations. *Anal. Chem.* **2008**, *80*, 4363−4372.

(4) Maier, N. M.; Franco, P.; Lindner, W. Separation of enantiomers: needs, challenges, perspectives. *J. Chromatogr. A* **2001**, *906*, 3−33.

(5) Yang, H.; Zheng, W. H. Recent advances on nonenzymatic catalytic kinetic resolution of diols. *Tetrahedron Lett.* **2018**, *59*, 583−591.

(6) Vedejs, E.; Jure, M. Efficiency in nonenzymatic kinetic resolution. *Angew. Chem., Int. Ed.* **2005**, *44*, 3974−4001.

(7) Kumar, S. P.; Nagaiah, K.; Chorghade, M. S. The first total synthesis of (S)-clavulazine from D-mannitol. *Tetrahedron Lett.* **2006**, *47*, 7149−7151.

(8) Bredikhin, A. A.; Bredikhina, Z. A. Stereoselective crystallization as a basis for single enantiomer drug production. *Chem. Eng. Technol.* **2017**, *40*, 1211−1220.

(9) Jiang, X.; Shao, Y.; Sheng, L.; Li, P.; He, G. Membrane crystallization for process intensification and control: a review. *Engineering* **2021**, *7*, 50−62.

(10) Liu, T.; Li, Z.; Wang, J.; Chen, J.; Guan, M.; Qiu, H. Solid membranes for chiral separation: A review. *Chem. Eng. J.* **2021**, *410*, 128247.

(11) Pinto, M. M.; Fernandes, C.; Tiritan, M. E. Chiral separations in preparative scale: a medicinal chemistry point of view. *Molecules* **2020**, *25*, 1931.

(12) You, Z. Y.; Liu, Z. Q.; Zheng, Y. G. Chemical and enzymatic approaches to the synthesis of optically pure ethyl (r)-4-cyano-3-hydroxybutanoate. *Appl. Microbiol. Biotechnol.* **2014**, *98*, 11−21.

(13) Coquerel, G.; Hoquante, M. Spontaneous and controlled macroscopic chiral symmetry breaking by means of crystallization. *Symmetry* **2020**, *12*, 1796.

(14) Medina, D. D.; Mastai, Y. Chiral polymers and polymeric particles for enantioselective crystallization. *Isr. J. Chem.* **2018**, *58*, 1330−1337.

(15) Abu Bakar, M. R.; Nagy, Z. K.; Saleemi, A. N.; Rielly, C. D. The impact of direct nucleation control on crystal size distribution in pharmaceutical crystallization processes. *Cryst. Growth Des.* **2009**, *9*, 1378−1384.

(16) Tulashie, S. K.; von Langermann, J.; Lorenz, H.; Seidel-Morgenstern, A. Chiral task-specific solvents for mandelic acid and their impact on solution thermodynamics and crystallization kinetics. *Cryst. Growth Des.* **2011**, *11*, 240−246.

(17) Polenske, D.; Lorenz, H.; Seidel-Morgenstern, A. Potential of different techniques of preferential crystallization for enantioseparation of racemic compound forming systems. *Chirality* **2009**, *21*, 728−737.

(18) Wu, T.; Zhu, J.; Wei, Q.; Li, P.; Wang, L.; Huang, J.; Wang, J.; Tang, L.; Wu, L.; Li, C.; Han, W. Preparative separation of four isomers of synthetic anisodamine by HPLC and diastereomer crystallization. *Chirality* **2019**, *31*, 11−20.

(19) Balawejder, M.; Kiwala, D.; Lorenz, H.; Seidel-Morgenstern, A.; Piatkowski, W.; Antos, D. Resolution of a diasteromeric salt of citalopram by multistage crystallization. *Cryst. Growth Des.* **2012**, *12*, 2557−2566.

(20) Tulashie, S. K.; Lorenz, H.; Seidel-Morgenstern, A. Potential of chiral solvents for enantioselective crystallization. 2. Evaluation of kinetic effects. *Cryst. Growth Des.* **2009**, *9*, 2387−2392.

(21) Preiss, L. C.; Werber, L.; Fischer, V.; Hanif, S.; Landfester, K.; Mastai, Y.; Munoz-Espi, R. Amino-acid-based chiral nanoparticles for enantioselective crystallization. *Adv. Mater.* **2015**, *27*, 2728−2732.

(22) Jaria, G.; Lourenco, M. A.; Silva, C. P.; Ferreira, P.; Otero, M.; Calisto, V.; Esteves, V. I. Effect of the surface functionalization of a waste-derived activated carbon on pharmaceuticals' adsorption from water. *J. Mol. Liq.* **2020**, *299*, 112098.

(23) Elfassy, E.; Basel, Y.; Mastai, Y. Crystallization of amino acids at the chiral ionic liquid/water interface. *CrystEngComm* **2016**, *18*, 8769−8775.

(24) Chen, B.; Deng, J.; Cui, X.; Yang, W. Optically active helical substituted polyacetylenes as chiral seeding for inducing enantioselective crystallization of racemic n-(tert-butoxycarbonyl) alanine. *Macromolecules* **2011**, *44*, 7109−7114.

(25) Zhou, K.; Tong, L.; Deng, J.; Yang, W. Hollow polymeric microspheres grafted with optically active helical polymer chains: preparation and their chiral recognition ability. *J. Mater. Chem.* **2010**, *20*, 781−789.

(26) Shen, Y.; Tian, G.; Huang, H.; He, Y.; Xie, Q.; Song, F.; Lu, Y.; Wang, P.; Gao, Y. Chiral self-assembly of nonplanar 10,10'-dibromo-9,9'-bianthryl molecules on Ag (111). *Langmuir* **2017**, *33*, 2993−2999.

(27) Wu, S.; Yin, Z.; Wu, D.; Tao, Y.; Kong, Y. Chiral enantioselective assemblies induced from achiral porphyrin by L- and D-lysine. *Langmuir* **2019**, *35*, 16761−16769.

(28) Qin, X.; Han, J.; Yang, D.; Chen, W.; Zhao, T.; Jin, X.; Guo, P.; Duan, P. Chiral self-assembly regulated photon upconversion based on triplet-triplet annihilation. *Chin. Chem. Lett.* **2019**, *30*, 1923−1926.

(29) Kuni, F. M.; Shchekin, A. K.; Grinin, A. P. Theory of heterogeneous nucleation for vapor undergoing a gradual metastable state formation. *Phys.-Usp.* **2001**, *44*, 331.

(30) Abyzov, A. S.; Schmelzer, J. W. P. Generalized Gibbs' approach in heterogeneous nucleation. *J. Chem. Phys.* **2013**, *138*, 164504.

(31) Di Profio, G.; Curcio, E.; Drioli, E. Supersaturation control and heterogeneous nucleation in membrane crystallizers: facts and perspectives. *Ind. Eng. Chem. Res.* **2010**, *49*, 11878−11889.

(32) Wang, S.; Feng, M.; Du, H.; Weigand, J. J.; Zhang, Y.; Wang, X. Determination of metastable zone width, induction time and primary nucleation kinetics for cooling crystallization of sodium orthovanadate from NaOH solution. *J. Cryst. Growth* **2020**, *545*, 125721.

(33) Zhao, Y.; Hou, G.; Kamaraju, V. K.; He, Y.; Power, G.; Glennon, B. Primary nucleation of benzoic acid in aqueous ethanol solution. *Ind. Eng. Chem. Res.* **2020**, *59*, 484−490.

(34) Lenka, M.; Sarkar, D. Determination of metastable zone width, induction period and primary nucleation kinetics for cooling crystallization of L-asparaginenohydrate. *J. Cryst. Growth* **2014**, *408*, 85−90.

(35) Shim, H. M.; Kim, J. K.; Kim, H. S.; Koo, K. K. Molecular dynamics simulation on nucleation of ammonium perchlorate from an aqueous solution. *Cryst. Growth Des.* **2014**, *14*, 5897−5903.

(36) Qiu, H.; Che, S. Tighter packing leads to higher enantiopurity: effect of basicity on the enantiopurity of N-acylamino acid-templated chiral mesoporous silica. *Chem. Lett.* **2010**, *39*, 70−71.

(37) An, C.-B.; Li, D.; Liang, R.; Bu, Y.-Z.; Wang, S.; Zhang, E.-H.; Wang, P.; Ai, X.-C.; Zhang, J.-P.; Skibsted, L. H. Chain length effects in isoflavonoid daidzein alkoxy derivatives as antioxidants: a quantum mechanical approach. *J. Agric. Food Chem.* **2011**, *59*, 12652−12657.

(38) Chen, Z.; Zhai, J.; Liu, X.; Mao, S.; Zhang, L.; Rohani, S.; Lu, J. Solubility measurement and correlation of the form A of ibrutinib in organic solvents from 278.15 to 323.15 K. *J. Chem. Thermodyn.* **2016**, *103*, 342−348.

(39) Fan, F.; Yuan, H.; Feng, Y.; Liu, F.; Zhang, L.; Liu, X.; Zhu, X.; An, W.; Rohani, S.; Lu, J. Molecular simulation approaches for the prediction of unknown crystal structures and solubilities of (R)- and (R,S)-crizotinib in organic solvents. *Cryst. Growth Des.* **2019**, *19*, 5882−5895.

(40) Liu, H.; Pierre-Pierre, N.; Huo, Q. Dynamic light scattering for gold nanorod size characterization and study of nanorod-protein interactions. *Gold Bull.* **2012**, *45*, 187−195.

(41) Bohström, Z.; Lillerud, K. P. Crystal growth kinetics of unseeded high silica chabazite. *J. Cryst. Growth* **2018**, *498*, 154−159.

(42) Fischer, A. T.; Compton, R. N.; Pagni, R. M. Solvent effects on the optical rotation of (S)-(−)-α-methylbenzylamine. *J. Phys. Chem. A* **2006**, *110*, 7067−7071.

(43) Extrand, C. W. Water contact angles and hysteresis of polyamide surfaces. *J. Colloid Interface Sci.* **2002**, *248*, 136−142.

(44) Wang, D.; Lu, J.; Zhang, L.; Fan, F.; Zhang, L.; Liu, X.; Yuan, H.; Zhu, X. Experimental and molecular dynamics simulation study on the primary nucleation of penicillamine racemate and its enantiomers in the mixture solvent of water and ethanol. *Ind. Eng. Chem. Res.* **2020**, *59*, 21957−21968.

(45) Ye, X.; Cui, J.; Li, B.; Li, N.; Zhang, J.; Wan, X. Self-reporting inhibitors: a single crystallization process to obtain two optically pure enantiomers. *Angew. Chem., Int. Ed.* **2018**, *57*, 8120−8124.

(46) Grimme, S.; Antony, J.; Ehrlich, S.; Krieg, H. A consistent and accurate ab initio parametrization of density functional dispersion correction (DFT-D) for the 94 elements H-Pu. *J. Chem. Phys.* **2010**, *132*, 154104.

(47) Berendsen, H. J. C.; Grigera, J. R.; Straatsma, T. P. The missing term in effective pair potentials. *J. Phys. Chem.* **1987**, *91*, 6269−6271.

(48) Berendsen, H. J. C.; van der Spoel, D.; van Drunen, R. GROMACS: a message-passing parallel molecular dynamics implementation. *Comput. Phys. Commun.* **1995**, *91*, 43−56.

(49) Lindahl, E.; Hess, B.; van der Spoel, D. GROMACS 3.0: a package for molecular simulation and trajectory analysis. *J. Mol. Model.* **2001**, *7*, 306−317.

(50) van der Spoel, D.; Lindahl, E.; Hess, B.; Groenhof, G.; Mark, A. E.; Berendsen, H. J. C. GROMACS: fast, flexible, and free. *J. Comput. Chem.* **2005**, *26*, 1701−1718.

(51) Hess, B.; Kutzner, C.; van der Spoel, D.; Lindahl, E. GROMACS 4: algorithms for highly efficient, load-balanced, and scalable molecular simulation. *J. Chem. Theory Comput.* **2008**, *4*, 435−447.

(52) Wang, J.; Wolf, R. M.; Caldwell, J. W.; Kollman, P. A.; Case, D. A. Development and testing of a general amber force field. *J. Comput. Chem.* **2004**, *25*, 1157−1174.

(53) Bussi, G.; Donadio, D.; Parrinello, M. Canonical sampling through velocity rescaling. *J. Chem. Phys.* **2007**, *126*, 014101.

(54) Li, W.; Liang, J.; Yang, W.; Deng, J. Chiral functionalization of graphene oxide by optically active helical-substituted polyacetylene chains and its application in enantioselective crystallization. *ACS Appl. Mater. Interfaces* **2014**, *6*, 9790−9798.

(55) Lee, T.; Lin, Y. K. The origin of life and the crystallization of aspartic acid in water. *Cryst. Growth Des.* **2010**, *10*, 1652−1660.

(56) Pinto, L. D.; Puppin, P. A.L.; Behring, V. M.; Flinker, D. H.; Merce, A. L. R.; Mangrich, A. S.; Rey, N. A.; Felcman, J. Solution and solid state study of copper (II) ternary complexes containing amino acids of interest for brain biochemistry-1: aspartic or glutamic acids with methionine or cysteine. *Inorg. Chim. Acta* **2010**, *363*, 2624−2630.

(57) Wu, J.; Wang, J.; Zhao, H. Solubility of d-aspartic acid in several neat solvents: determination, modeling, and solvent effect analysis. *J. Chem. Eng. Data* **2019**, *64*, 2904−2910.

(58) Sandhu, R. K.; Kaur, A.; Kaur, P.; Rajput, J. K.; Khullar, P.; Bakshi, M. S. Solubilization of surfactant stabilized gold nanoparticles in oil-in-water and water-in-oil microemulsions. *J. Mol. Liq.* **2021**, *336*, 116305.

(59) Kim, K. J.; Mersmann, A. Estimation of metastable zone width in different nucleation processes. *Chem. Eng. Sci.* **2001**, *56*, 2315−2324.

(60) Trabelsi, S.; Tlili, M.; Abdelmoulahi, H.; Bouazizi, S.; Nasr, S.; Gonzalez, M. A.; Bellissent-Funel, M.-C.; Darpentigny, J. Intermolecular interactions in an equimolar methanol-water mixture: neutron scattering, DFT, NBO, AIM, and MD investigations. *J. Mol. Liq.* **2022**, *349*, 118131.

(61) Zhu, S. F.; Gan, Q.; Feng, C. Multimolecular complexes of CL-20 with nitropyrazole derivatives: geometric, electronic structure, and stability. *ACS Omega* **2019**, *4*, 13408−13417.

(62) Bai, Q.; Yao, X. Investigation of allosteric modulation mechanism of metabotropic glutamate receptor 1 by molecular dynamics simulations, free energy and weak interaction analysis. *Sci. Rep.* **2016**, *6*, 21763.

(63) Ye, X.; Cui, J.; Li, B.; Li, N.; Wang, R.; Yan, Z.; Tan, J.; Zhang, J.; Wan, X. Enantiomer-selective magnetization of conglomerates for quantitative chiral separation. *Nat. Commun.* **2019**, *10*, 1964.